JCTC Journal of Chemical Theory and Computation

pubs.acs.org/JCTC Article

Spin-Vibronic Intersystem Crossing and Molecular Packing Effects in Heavy Atom Free Organic Phosphor

Published as part of Journal of Chemical Theory and Computation virtual special issue "First-Principles Simulations of Molecular Optoelectronic Materials: Elementary Excitations and Spatiotemporal Dynamics".

Thomas Pope, Julien Eng, Andrew Monkman, and Thomas J. Penfold*

Cite This: J. Chem. Theory Comput. 2024, 20, 1337−1346

ABSTRACT: We present a detailed investigation into the excited state properties of a planar D_{3h} symmetric azatriangulenetrione, HTANGO, which has received significant interest due to its high solid-state phosphorescence quantum yield and therefore potential as an organic room temperature phosphorescent (ORTP) dye. Using a model linear vibronic coupling Hamiltonian in combination with quantum dynamics simulations, we observe that intersystem crossing (ISC) in HTANGO occurs with a rate of $\sim 10^{10}$ s^{-1}, comparable to benzophenone, an archetypal molecule for fast ISC in heavy metal free molecules. Our simulations demonstrate that the mechanism for fast ISC is associated with the high density of excited triplet states which lie in close proximity to the lowest singlet states, offering multiple channels into the triplet manifold facilitating rapid population transfer. Finally, to rationalize the solid-state emission properties, we use quantum chemistry to investigate the excited state surfaces of the HTANGO dimer, highlighting the influence and importance of the rotational alignment between the two HTANGO molecules in the solid state and how this contributes to high phosphorescence quantum yield.

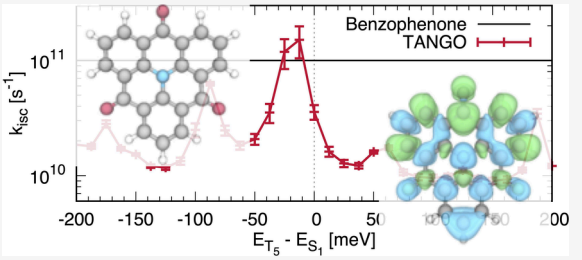

INTRODUCTION

Purely organic molecules exhibiting a strong coupling between the singlet and triplet manifolds have attracted a significant research effort in both fundamental[1−7] as well as applied research fields.[8−12] Indeed, for the latter, organic molecules which display efficient population transfer between singlet and triplet states have the potential to be applied as key components in organic light emitting diodes operating via thermally activated delayed fluorescence[8,13−15] or in photodynamic therapy,[16,17] photocatalysts[18−20] and molecular logic gates.[21] Besides excited state switching between singlet and triplet states, there is also a surging interest in organic room temperature phosphorescent dyes as substitutes for conventional inorganic or metal−organic phosphors.[9,22−25]

In most organic molecules, the coupling between the singlet and triplet manifolds is weak, making intersystem crossing (ISC) and phosphorescence uncompetitive compared to spin-allowed transitions such as fluorescence and nonradiative decay.[26,27] The simplest approach for enhancing spin state mixing is by increasing spin−orbit coupling (SOC) through the heavy-atom effect by incorporating atoms such as Br or I into the material.[28,29] However, alternative approaches have sought to exploit the twist in the molecular structure[7,30−33] and increase the density of low lying triplet excited states.[34−38] Alternatively, as outlined by El-Sayed,[39,40] SOC can be enhanced by tuning the character of the states involved. To achieve effective SOC, any change in spin must be accompanied by a corresponding change in orbital angular momentum, so that total angular momentum is conserved and such conditions are fulfilled by coupling $n-\pi^*$ and $\pi-\pi^*$ states, which can be realized using carbonyl (C═O) containing derivatives.

One of the most widely studied examples of ISC dynamics in heavy metal free organic molecules is benzophenone, which exhibits ISC in the picosecond regime.[42−47] Excited state dynamics simulations of benzophenone performed by Favero et al.[48] demonstrated that direct (i.e., $S_1 \rightarrow T_1$) ISC accounted for the majority of the spin-flipping dynamics, with the remaining crossing to the T_2 or higher triplet states, which subsequently undergo ultrafast nonradiative decay into the T_1 state. Their simulations ascribed the fast ISC to two internal coordinates activated after $n-\pi^*$ excitation, namely, the C═O stretch and the torsion of phenyl rings. Further supporting this,

Received: November 3, 2023
Revised: January 4, 2024
Accepted: January 4, 2024
Published: January 25, 2024

Karak et al.[49] recently demonstrated that quenching of the latter (i.e., the torsion of phenyl rings) using the fused analogue of benzophenone, fluorenone, reduced the rate of ISC by 3 orders of magnitude.

In 1971, Hellwinkel et al.[50] synthesized a series of azatriangulenetriones, the archetypal of which is shown in Figure 1 and from now on will be referred to as HTANGO.

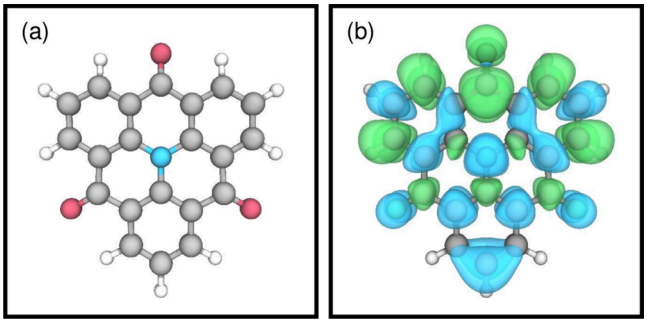

Figure 1. (a) Representation of the structure of the unsubstituted azatriangulenetriones, HTANGO.[41] (b) Difference of electronic density associated with the $S_0 \rightarrow S_1$ transition at the ground state geometry.

The crystal structure was determined by Field and Venkataraman,[51] and related complexes have recently been synthesized with the objective of achieving molecules which exhibit narrow emission for application in OLEDs.[52,53] Hamzehpoor and Perepichka[41] have studied the luminescent properties of HTANGO and related derivatives in solution and the solid state. Despite the rigidity of the structure, found to be detrimental for the ISC of benzophenone, the authors demonstrated that HTANGO exhibited a solid-state phosphorescence quantum yield of 42% at room temperature and is the most efficient phosphor composed of first- and second-row elements only. Consequently, toward achieving a detailed understanding of its photophysics, especially in the context of ISC and phosphorescence, in this work, we combine quantum chemistry and quantum dynamics to study the excited state dynamics of HTANGO. We show, employing a model linear vibronic coupling Hamiltonian and conducting quantum dynamics simulations, that HTANGO undergoes ISC with a rate of approximately 10^{10} s^{-1}, comparable to benzophenone, driven by exploiting the high density of low lying triplet excited states. Additionally, we employ quantum chemistry to explore the excited state surfaces of HTANGO dimers and emphasize the significance of rotational alignment between HTANGO monomers to elucidate the solid-state emission properties. Overall, this study provides valuable insights into the excited state behavior of HTANGO leading to potential applications as an ORTP dye.

THEORY

Quantum Chemistry. All density functional theory (DFT), time-dependent density functional theory (TD-DFT), and equation-of-motion coupled cluster (EOM-CCSD) theory calculations were performed with the ORCA 5 quantum chemistry package.[54−56] All calculations employed a def2-TZVP basis set and, where applicable, the corresponding auxiliary /C and /J basis sets.[57,58] A linear-response conductor-like polarizable continuum model with the properties of chloroform was used in all cases.[59] DFT/TD-DFT simulations were performed within the approximation of the PBE0 exchange-correlation functional[60,61] and a pairwise dispersion correction.[62,63] All TD-DFT calculations were performed within the Tamm−Dancoff approximation.[64]

Linear Vibronic Coupling Hamiltonian. The Linear Vibronic Coupling (LVC) Hamiltonian[65,66] has previously been widely used to study the photophysics,[67−70] including intersystem crossing[71−75] of molecular systems. It comprises a base Hamiltonian and four additional terms defining four coupling mechanisms,

$$\mathcal{H}^{\mathrm{LVC}} = \mathcal{H}^{0} + \mathcal{H}^{\eta} + \mathcal{H}^{\kappa} + \mathcal{H}^{\lambda} + \mathcal{H}^{\gamma} \tag{1}$$

The base Hamiltonian for the system is constructed from the normal modes Q_k, their frequencies ω_k, and the vertical excitation energies ϵ_n.

$$\mathcal{H}^{0} = \sum_{n} \left[\epsilon_n + \sum_{k} \frac{\omega_k}{2} \left(-\frac{\partial^2}{\partial Q_k^2} + Q_k^2 \right) \right] |n\rangle\langle n| \tag{2}$$

The spin−orbit coupling (SOC) η^{mn} is calculated using quasi-degenerate perturbation theory[76] and the gradient of the spin−orbit coupling with respect to the normal modes $\partial\eta^{mn}/\partial Q_i$ is estimated using a finite-difference method. [Note: Here, the molecule is displaced along the normal mode by increments of 0.1 dimensionless normal coordinates. The gradient is calculated with a linear fit.] With these components, the SOC Hamiltonian is given,

$$\mathcal{H}^{\eta} = \sum_{m,n} \left[\eta^{mn} + \sum_{k} \frac{\partial \eta^{mn}}{\partial Q_k} Q_k \right] |m\rangle\langle n| + h.c. \tag{3}$$

Owing to the D_{3h} point group symmetry of the HTANGO molecule, three LVC terms are considered. For fully symmetric normal modes, intrastate coupling, κ_n, is included for all states,

$$\mathcal{H}^{\kappa} = \sum_{n} \sum_{k} \kappa_k^n Q_k |n\rangle\langle n| \tag{4}$$

Otherwise, when the direct product between the irreducible representations (irreps) of the electronic states, $\Gamma_{m/n}$, and the normal modes, Γ_{Q_k}, contains the fully symmetric irrep ($\Gamma_m \otimes \Gamma_{Q_k} \otimes \Gamma_n \supseteq \Gamma_{A_1'}$), interstate vibronic coupling, λ_k^{mn}, is induced,

$$\mathcal{H}^{\lambda} = \sum_{m,n} \sum_{k} \lambda_k^{mn} Q_k |m\rangle\langle n| \tag{5}$$

with the exception of degenerate states of E' or E'' symmetry. In this case, the pair of states, n and n', is coupled by a degenerate pair of normal modes, k and k', via Jahn−Teller (JT) coupling,

$$\mathcal{H}^{\gamma} = \sum_{n} \sum_{k} \gamma_k^n [(|n\rangle\langle n| - |n'\rangle\langle n'|) Q_{k'} - |n\rangle\langle n'| Q_k + h.c.] \tag{6}$$

We consider the lowest singlet states, the degenerate pair S_1/S_2, and the eight triplet states of similar or lower energy. Of the triplet states, there are three degenerate pairs, T_1/T_2, T_3/T_4, and T_7/T_8, and two nondegenerate states, T_5 and T_6. Figure 2 shows a schematic of the states and the coupling pathways available. The spin−orbit coupling induces transfer between the singlet states and T_3/T_4 and T_5 states. The higher triplet states all couple through the e' modes and the triplet pair T_1/T_2 couples to the higher triplet states through e'' modes. JT

https://doi.org/10.1021/acs.jctc.3c01220
J. Chem. Theory Comput. 2024, 20, 1337−1346

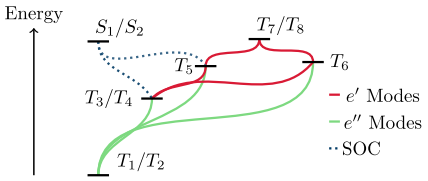

Figure 2. Schematic of the HTANGO monomer and the coupling pathways through spin−orbit coupling (blue-dashed) and LV coupling through the e' (red) and e'' (green) modes. The states are vertically distributed following their energies.

coupling occurs between degenerate pairs of states along e' modes.

Intrastate coupling terms are derived from the Franck−Condon (FC) geometry using the method outlined by Eng et al.[77] The JT terms were calculated in the same way, using the gradient of the adiabatic state at the FC geometry.

For interstate coupling, the approach was modified. In the standard approach, the interstate coupling between two states is given by the second derivatives along the normal modes for each state involved,

$$\lambda_k^{mn} = \sqrt{\frac{|V_n - V_m|}{4}\left(\left.\frac{\partial^2 V_n}{\partial Q_k^2}\right|_{Q_0} - \left.\frac{\partial^2 V_m}{\partial Q_k^2}\right|_{Q_0}\right)} \tag{7}$$

However, this two-state approach assumes the change in gradient along a normal mode for a given state is caused by only one other state, which is not always the case, especially for molecules exhibiting a high density of states. For example in the present case of HTANGO, as shown in Figure 2, T_6 (which has A_1' symmetry) is expected to vibronically couple to two degenerate pairs, T_3/T_4 and T_7/T_8 (both of E' symmetry), via e' modes. This vibronic coupling via a given mode leads to a repulsion between the states along that mode, which increases the gradiant for states coupled to lower-energy states, and decreases the gradient for states coupled to higher-energy states. In the above case, we would expect the gradient of the T_5 energy to be increased due to the T_3/T_4 pair and reduced due to the T_7/T_8 and, since these behaviors will both be observed, the change in gradient for this state along any e' will not be a reliable metric. In eq 7, the change in any two coupled states is expected to be equal and opposite. Consequently, and accounting for the underlying parabolic behavior of the ground state, we can rewrite the equation to depend on only one state,[68]

$$\lambda_k^{mn} = \sqrt{\frac{|V_n - V_m|}{2}\left(\left.\frac{\partial^2 V_n}{\partial Q_k^2}\right|_{Q_0} - \omega_k\right)} \tag{8}$$

The interstate coupling is then calculated by either eq 7 or eq 8 depending on how reliable the second derivatives are expected to be. Generally, we use eq 7 unless one of the states has no other couplings that could lead to a change in gradient. In addition, given that most states under consideration are degenerate, all the coupling terms are multiplied by a factor of 1/2, to avoid double counting.

Quantum Dynamics. Quantum dynamics were performed using the Quantics 1.2[78] implementation of the multiconfigurational time-dependent Hartree (MCTDH) method.[79,80] The dynamics were performed using four model Hamiltonians. The first (model A) includes the two lowest singlet states and the eight lowest triplet states coupled with all terms described in this paper. Model B incorporates the same states, but removes the spin−orbit coupling gradients, i.e., the SOC is independent of Q and fixed to that at the FC geometry. Model C retains the SOC gradient, but removes the highest-lying triplet states (T_6−T_8). Finally, model D incorporates the same states as model A, but substitutes the state energies as calculated with EOM-CCSD.

Each normal mode in the model is described using 41 harmonic oscillator eigenfunction basis. To reduce the computational expense, mode pairs (ν_5:ν_6, ν_{21}:ν_{22}, ν_{23}:ν_{24}, ν_{72}:ν_{73}, and ν_{19}:ν_{50}) are contracted into a single degree of freedom. Simulations are run within the multistate formalism, and 12 single-particle functions are used for each singlet and triplet state. These ensure convergence during the simulations presented herein. The initial wave function is built using one-dimensional harmonic oscillator functions with zero initial momentum and is vertically excited into the S_1 state at the FC geometry.

RESULTS

Excited State Properties and Spin−Orbit Coupling of HTANGO. Table 1 shows the TD-DFT(PBE0) and EOM-CCSD computed excited state energies of HTANGO at critical geometries on the ground and excited state potential energy surfaces. At the ground state (S_0) optimized geometry the

Table 1. Excited State Energies at the Ground State and Lowest Singlet and Triplet Excited States Optimized Geometries of HTANGO

	S_0				S_1		T_1	
	TD-DFT		EOM-CCSD		TD-DFT		TD-DFT	
	E_i [eV]	f_{osc}	E_i [eV]	f_{osc}	E_i [eV]	f_{osc}	E_i [eV]	f_{osc}
$S_1(E')$	3.41	0.20	3.31	0.20	3.27	0.19	3.24	0.21
$S_2(E')$	3.41	0.20	3.30	0.20	3.38	0.21	3.33	0.19
$T_1(E')$	2.79	-	2.89	-	2.66	-	2.56	-
$T_2(E')$	2.79	-	2.89	-	2.73	-	2.71	-
$T_3(E'')$	3.15	-	3.42	-	3.01	-	2.90	-
$T_4(E'')$	3.15	-	3.41	-	3.10	-	3.06	-
$T_5(A_1'')$	3.30	-	3.52	-	3.21	-	3.16	-
$T_6(A_1'')$	3.32	-	3.14	-	3.19	-	3.14	-
$T_7(E'')$	3.43	-	3.32	-	3.31	-	3.25	-
$T_8(E'')$	3.43	-	3.30	-	3.39	-	3.34	-

https://doi.org/10.1021/acs.jctc.3c01220
J. Chem. Theory Comput. 2024, 20, 1337−1346

lowest lying singlet and triplet states in TANGO are degenerate pairs of E' symmetry, with the density difference associated with the S_1 state shown in Figure 1b.

At the ground state geometry, the lowest singlet states of HTANGO, computed using TD-DFT, are at 3.41 eV, which is in good agreement with EOM-CCSD but higher than the 3.10 eV (400 nm) observed in the experimental absorption spectrum in ref 41. Both the TD-DFT and EOM-CCSD calculations exhibit 8 triplet states below or within close proximity to the degenerate S_1/S_2 pair, which would be favorable for ISC. At the lowest singlet excited state optimized geometry, related to the fluorescence properties, the S_1 state is at 3.27 eV, indicating a Stokes shift of 0.14 eV in good agreement with experiment. Despite the structural rearrangement, which lifts the degeneracy of the S_1/S_2 states, there remains a high density of triplet states lower than the S_1 state. The lowest triplet state at the triplet geometry, corresponding to the phosphorescence properties, exhibits an energy of 2.56 eV, in excellent agreement with the experimentally recorded phosphorescence 475 nm (2.61 eV).

Table 2 shows the spin−orbit coupling matrix elements (SOCME) calculated between the low-lying excited states. As expected for a purely organic molecule, the coupling is generally weak with all couplings between singlet and triplet states ≤10 cm^{-1}. While larger SOCME exist between the triplet states, these are all small when compared to the calculated diabatic couplings (λ, see Table S3) and will therefore not play a significant role during the dynamics. Table 3 compares the nonzero SOCME between the singlet and triplet states for HTANGO to both benzophenone and fluorenone. The SOCME of HTANGO are substantially smaller than those of benzophenone, due to the constrained planar structure,[49] however, owing to the degeneracy of the S_1 and S_2 and the T_3 and T_4 states, HTANGO has six coupling pathways, whereas, for benzophenone, there are two. Consequently, while the SOCME are smaller in HTANGO than in benzophenone, the existence of three times as many pathways could be expected to somewhat compensate for the smaller SOCME.[36] The SOCME in HTANGO is significantly higher than that of fluorenone. Consequently, while the rigid planarity of HTANGO clearly reduces the SOCME, compared to benzophenone, its high symmetry facilitates the multiple pathways which are likely to encourage ISC.

Table 2. All Non-zero Spin−Orbit Couplings in cm^{-1} at the Ground State Optimized Geometry of HTANGO

	T_2	T_3	T_4	T_5	T_6	T_7	T_8
S_1	-	6.4	6.2	10.3	-	-	-
S_2	-	6.0	6.2	10.5	-	-	-
T_1	0.1	15.8	15.4	22.5	-	0.1	-
T_2	-	15.1	15.3	22.9	-	-	0.1
T_3	-	-	2.8	-	29.4	9.2	9.2
T_4	-	-	-	-	29.3	9.3	9.5
T_5	-	-	-	-	0.3	8.2	7.9

Table 3. Summary of the SOC Pathways in the HTANGO Molecule Compared to Similar Molecules Studied by Karak *et al.*[49]

Molecule	Pathway	SOCME (cm^{-1})	ΔE (eV)
Benzophenone	$S_1 \rightarrow T_2$	52.6[49]	0.14[49]
	$S_1 \rightarrow T_1$	23.3[49]	0.62[49]
HTANGO	$S_1 \rightarrow T_5$	10.3	0.11
	$S_2 \rightarrow T_5$	10.5	0.11
	$S_1 \rightarrow T_4$	6.2	0.26
	$S_1 \rightarrow T_4$	6.2	0.26
	$S_1 \rightarrow T_3$	6.4	0.26
	$S_2 \rightarrow T_3$	6.0	0.26
Fluorenone	$S_1 \rightarrow T_2$	0.56[49]	0.50[49]
	$S_1 \rightarrow T_1$	2.10[49]	0.60[49]

Developing the Linear Vibronic Coupling Hamiltonian. Having established the excited state properties, we now seek a more detailed insight into the excited state processes using quantum dynamics, which requires a Hamiltonian. HTANGO has 34 atoms and therefore 96 normal modes. Consequently, calculating the full PES is unrealistic. To reduce the computational effort we use a reduced space Hamiltonian, based upon the linear vibronic coupling model. The validity of the linear vibronic coupling Hamiltonian in this case is based upon the assumption that the rigidity of HTANGO means that anharmonicity of the potential energy surfaces does not play a significant role in the dynamics. To assess the accuracy, we use the recently introduced Global Anharmonicity Parameter[77] (GAP), which in the S_1 state is 5% and in the T_1 state is 13%. A GAP of around 10% suggests that anharmonicity effects are small and the LVC potential can be considered a reliable approximation. While the T_1 state slightly exceeds this value, we note that the majority of this is due to the effect of the JT coupling, which gives rise to a gradient at the FC geometry in the state energies and inflates the GAP.[77] In addition, the geometries predicted by the LVC model are very similar to the fully optimized structures, with the RMSD of the T_1 state being 0.007 Å.

Figure 3 shows cuts of the potential energy curves along selected modes, with the remaining modes used in the Hamiltonian included in Figure S1. The green points represent the potentials reproduced using the LVC parameters, while the blue and red lines represent the potentials calculated using TD-DFT(PBE0). Overall, these plots reveal good agreement between the LVC model and the TD-DFT calculations, indicating that the LVC represents a good approximation for the potential energy surface.

In total ten normal modes were considered important for the LVC Hamiltonian, an assessment which was based upon the magnitude of the first-order coupling terms (see Tables S4 and S5 in the Supporting Information) and these include three degenerate pairs and two fully symmetric modes. The two a_1' modes chosen are ν_{19} and ν_{50}. ν_{19} has the largest intrastate couplings of any low-lying mode and the effect of this can be observed in Figure 3, which shows the excited state potentials shifted with respect to the ground state potential, illustrated with the dashed line. This shift is responsible for driving excited state dynamics as well as causing broadening, through vibronic structure, to the emission spectrum.[81] In contrast, ν_{50} is chosen as it has the largest difference in intrastate couplings between the singlet pair and the energetically nearby triplet states, effectively lowering the energy gap upon distortion along this mode.

Two pairs of e' modes are selected to allow for coupling within degenerate pairs and between the upper triplet states (see Figure 2). Modes ν_{21}:ν_{22} are selected as they are the lowest lying e' modes with a significant JT coupling. This can be observed in Figure 3 as the splitting of the degenerate states as you move away from the Franck−Condon geometry. ν_{72}:ν_{73}

https://doi.org/10.1021/acs.jctc.3c01220
J. Chem. Theory Comput. 2024, 20, 1337−1346

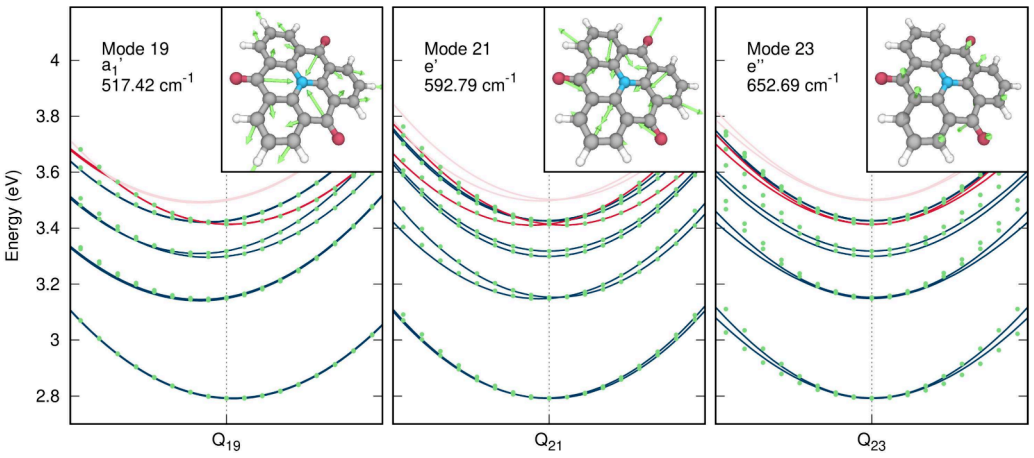

Figure 3. Energy of the singlet (red) and triplet (blue) states as the molecule is projected along representative modes considered in the dynamics in dimensionless normal coordinates (similar plots for the other modes used in the dynamics are shown in the SI). The green points represent the energy levels given by the LVC Hamiltonian along the normal modes. The inset image shows the mode on the molecule

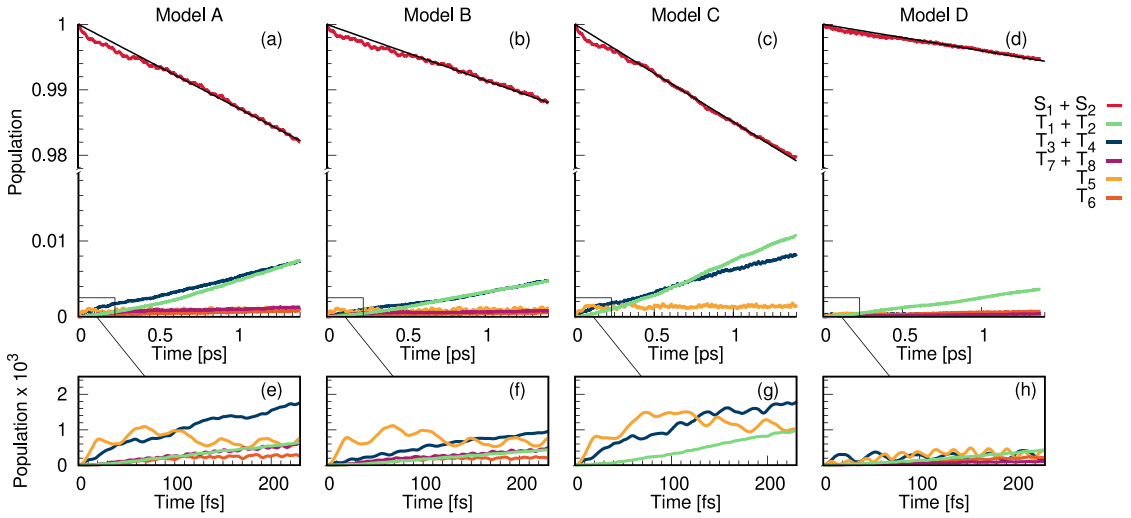

Figure 4. Population kinetics of the singlet and triplet states for the first 1.5 ps after excitation into S_1 for the full model Hamiltonian (a), the case where SOC gradients have been removed (b), the case where the three highest lying triplet states have been removed (c), and the case where the EOM-CCSD state energies have been used in place of the TDDFT energies (d). The initial dynamics for the first 200 fs are shown in (e)−(h) for the same models, respectively.

were selected because, of all the e' pairs, they induce the largest JT coupling (see SI). These modes also contribute a significant coupling between the high-lying triplet states as shown in Table 5 in the Supporting Information. Finally, to couple the high-lying triplet cluster to the lowest degenerate triplet pair, we use a pair of modes of e'' symmetry. Here, modes ν_5:ν_6 and ν_{23}:ν_{24} were chosen because they have the largest average coupling of any low-lying mode.

Quantum Dynamics. Having developed the excited state potential, using the LVC Hamiltonian, we now use this to study the ISC dynamics of HTANGO. Figure 4a shows the population kinetics of the singlet and triplet states for the first 1.5 ps after excitation into the lowest singlet excited state (S_1). This dynamics (Model A) includes all the couplings described in the previous sections. By fitting the decay of the population kinetic of the singlet states, we observe a $k_{ISC}^{A} = 1.3 \times 10^{10}$ s^{-1}, which is comparable to the k_{ISC} reported for benzophenone of $\sim 10^{11}$ s^{-1} and therefore very fast for an organic molecule. To elucidate the mechanism of the ISC, we modify this model to identify the most important pathways.

Figure 4b shows the same dynamics, but with the SOC gradients removed. This shows a reduction in the ISC rate, $k_{ISC}^{B} = 0.85 \times 10^{10}$ s^{-1}, highlighting that Herzbeg−Teller interactions play an important role. However, as the rate of ISC remains high, the primary mechanism for this intersystem crossing is the direct spin-allowed transitions. Figure 4c shows the dynamics for the model in which the three highest triplet states (T_6, T_7, and T_8) have been removed. Here, the fitted intersystem crossing rate, $k_{ISC}^{C} = 1.5 \times 10^{10}$ s^{-1}, is similar to the model with all states included, suggesting that the higher lying states do not play a significant role in the dynamics. For all models, the population kinetics of the triplet states is shown for the first 200 fs in Figures 4e−h. The populations of T_3, T_4, and T_5 rise the fastest in all cases as these are directly coupled and degenerate with the S_1 and S_2 states. The population then rises in the remaining triplet states as it transfers from the T_3, T_4, and T_5 states via vibronic coupling.

The above dynamics reveal the importance of coupling to the T_5 state. A key driving force for this is the close nature of the S_1/S_2 state with the T_5 state, with the T_5 appearing 0.11 eV

https://doi.org/10.1021/acs.jctc.3c01220
J. Chem. Theory Comput. 2024, 20, 1337−1346

below the singlet degenerate pair at the ground state geometry. However, as shown in Table 1, the ordering of the states changes in EOM-CCSD and the singlet states are closer to the states with weak or zero coupling. The T_5 state (calculated with TDDFT) with the larger SOC now occurs 0.21 eV higher in energy than the singlet states when calculated using EOM-CCSD. As shown in Figure 4d (Model D) this reduces the population transfer and therefore the ISC rate to $k_{ISC}^{A} = 0.4 \times 10^{10}$ s^{-1}. To further study this effect, we calculated the population dynamics for a range of Hamiltonians where all the parameters are taken from the model A Hamiltonian with the exception of the energy of the T_5 state, which is scanned from 0.2 eV below the energy of the lowest singlet pair to 0.2 eV above. Figure 5 shows the fitted ISC rates for the range of

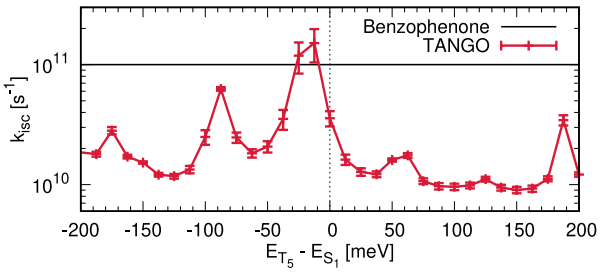

Figure 5. Intersystem-crossing rates calculated for the Model A Hamiltonian as a function of the energy difference between T_5 and S_1. For context, the k_{ISC} for benzophenone is shown as reported by Karak et al.[49]

Hamiltonians. Here, we see that the ISC depends strongly on the relative energy of the S_1 and T_5 states and indeed, if the states are degenerate, the ISC is nearly an order of magnitude higher than that predicted by the TD-DFT and EOM-CCSD state energies. This demonstrates that relatively small changes in structure, which bring the energy of the S_1 and T_5 states closer together, can have a dramatic effect on the dynamics, and this was used as a design principle to enhance the ISC rate in these molecules. To illustrate the importance of subtle structural changes, *ab initio* molecular dynamics calculations performed in the electronic ground state (see Figure S8) show that even at 77 K, the difference in energy between the T_5 and S_1 can fluctuate significantly, with a standard deviation of 31 meV over a 1 ps range, meaning using thermal energy alone, the system has sufficient energy to traverse the potential reaching regions where the T_5 and S_1 states are close in energy.

Electronic Structure of Dimer. The previous section has used quantum dynamics to investigate the ISC dynamics of the isolated monomer, highlighting an ISC rate comparable to benzophenone despite the rigidity of the structure. In ref 41, the authors demonstrated a significant difference between solution and crystal emission properties. Indeed, with low concentration in chloroform solution, the emission maximum is at ~425 nm (2.92 eV) slightly lower than the values calculated above in Table 1 (3.27 eV). However, in the solid state the prompt and delayed emission maxima redshift to 550 nm (2.25 eV). This was proposed to be the formation of π-stack dimers which can be hindered using bulky substituents.

To shed further light on the role of crystal packing on the excited state properties, Figure 6 shows the potential energy surfaces of the dimer around the excited S_1 geometry as a function of the angle, distance, and horizontal displacement between each monomer unit with respect to the other, consequently addressing the energetic landscape of potential J-, H-, and X-aggregates in the present system.[82] A schematic of the dimer structure used is shown in Figure S9. Figure 6a shows only the S_1 and T_1 states as a function of the angle and distance between the monomer units. These potentials exhibit two distinct minima in each state along dimer angles of 10° and 60°. The energy of the T_1 state at 10° is 2.24 eV, in excellent agreement with the emission spectrum of 2.25 eV (550 nm) reported in ref 41. In addition, the spectra in ref 41 show a small shoulder at around 470 nm (2.63 eV), close to the 2.58 eV of the singlet state at 10°. While the former has a very small oscillator strength (indicated by colored dots) compared to the singlet state minimum at 60° it is the lowest energy state, and therefore after vibrational cooling, the molecule can reside in this minima from where it can either

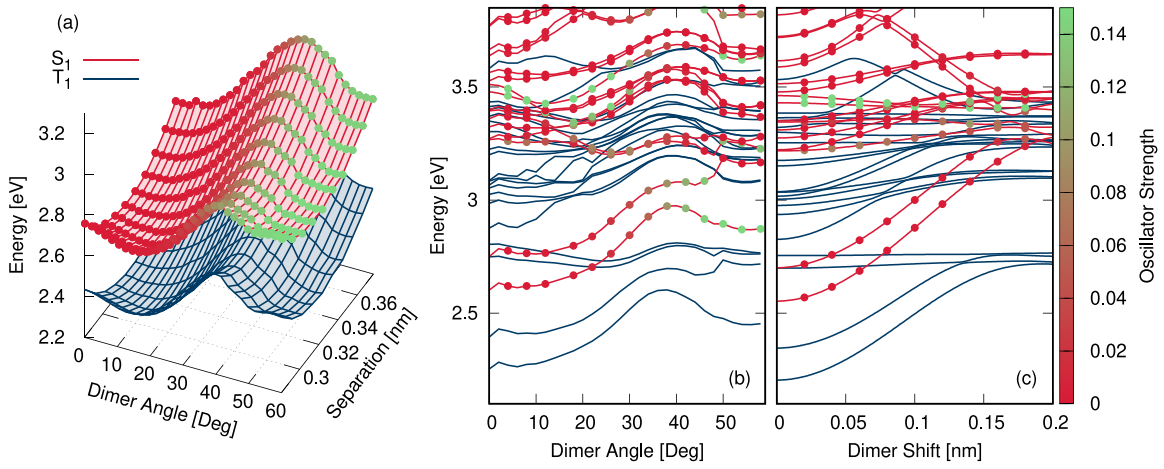

Figure 6. (a) Energy of the S_1 (red) and T_1 (blue) states for a range of dimer systems of varying angles and separation. In each system, the dimer angle and separation is constrained and the systems are otherwise optimized into the S_1 geometry. (b) Energy of the low-lying singlet (red) and triplet (blue) states for a range of dimer systems with varying angles. The dimer angle is constrained and the systems are otherwise optimized into the S_1 geometry. (c) Energy of the low-lying singlet (red) and triplet (blue) states for a range of dimer systems horizontally displaced from the low-angle minimum position. In all cases, the oscillator strength of the singlet states is shown as colored points on the surface, where red (green) points correspond to low (high) strengths.

https://doi.org/10.1021/acs.jctc.3c01220
J. Chem. Theory Comput. 2024, 20, 1337−1346

emit or undergo ISC. Indeed, assuming a thermal equilibrium between two S_1 minima, the relative intensity of each band, at room temperature, would be

$$\frac{Int(S_1^{60^\circ} \rightarrow S_0)}{Int(S_1^{10^\circ} \rightarrow S_0)} = \frac{f(S_1^{60^\circ} \rightarrow S_0)}{f(S_1^{10^\circ} \rightarrow S_0)} \cdot \exp\left(-\frac{\Delta E_{S_1^{60^\circ} - S_1^{10^\circ}}}{k_b T}\right) \quad (9)$$

Given the energy gap between the two minima of 0.26 eV, $f(S_1^{10^\circ}) = 0.00002$ and $f(S_1^{60^\circ}) = 0.14$, the ratio, $Int(S_1^{60^\circ} \rightarrow S_0)/Int(S_1^{10^\circ} \rightarrow S_0)$, is 0.3 at 300 K, meaning emission from $S_1^{10^\circ}$ will be about 3 times larger than $S_1^{60^\circ}$. Importantly, the steady state emission spectra reported in ref 41 show two weak shoulders at 450 and 470 nm, corresponding to 2.76 and 2.63 eV. These exhibit an ∼1:3 ratio, consistent with the above analysis, and we therefore assign them to the $S_1^{60^\circ}$ and $S_1^{10^\circ}$, respectively.

The shape of the dimer potential energy surface and the oscillator strength increasing with the angle between the monomer units can be further understood in Figure 6b, which shows all of the low-lying excited states in a one-dimensional cut. This shows that along the dimer angle, the low-lying singlet states intersect the higher-lying triplet states, which would be expected to enhance ISC.[83] This combined with the rigidity of the structure leading to a low nonradiative rate will be a strong contributing factor to the high phosphorescence yield, supporting the observations made by Hamzehpoor *et al.*[41] In addition, this clearly shows that although the rotated dimers (X-aggregate) have the largest oscillator strength, the lower energy structure is the structure for the 10°, *pseudo* H-aggregate, which is at 2.58 eV while the higher energy minimum at 60° is at 2.80 eV (443 nm). A similar thing is observed for the lowest triplet states which are at 2.3 eV (539 nm) at 10° and 2.48 eV (517 nm) for 60°. Finally, Figure 6c shows the potentials along the horizontal displacement between the two dimer units, i.e., differentiating between J- and H-aggregation. This clearly shows for the S_1 and T_1 states that a single minimum for the 0 dimer shift is observed, i.e., the excited state favors H-aggregation. Interestingly, the T_3 and T_4 excited states exhibit very little dependence on this shift leading to another crossing between these states and the lowest two singlet states.

In the solid state, the presence of monomeric states as well as dimeric (and potentially high-order) states competing with the multitude of close lying singlet and triplet states which both have multiple emissive configurations (*i.e., rotation of dimer angles*) means the solid state excited state dynamics of this system is likely to be complicated with many competing pathways. However, overall, the present simulations highlight the importance of intramolecular interactions for describing the phosphorescence properties, consistent with ref 24, which illustrated the special role of molecular dimers in persistent RTP emission.

DISCUSSION AND CONCLUSIONS

In this work we have performed a detailed computational investigation into the excited state properties of the planar D_{3h} symmetric azatriangulenetrione, HTANGO, with the focus of understanding the ISC and effect of intramolecular interactions which influences its performance as an organic room temperature phosphorescent (ORTP) dye.

Our quantum dynamics have demonstrated that HTANGO exhibits fast intersystem crossing (ISC) with a rate comparable to benzophenone. While the planar rigid structure of HTANGO appears to reduce the SOCME, compared to benzophenone, the high symmetry gives rise to a high density of triplet excited states in close proximity to the lowest singlet states, facilitating rapid population transfer. Among all of these states, the proximity of the T_5 state to S_1 in particular is identified as most significant to the rapid ISC.

Using quantum chemistry simulations of a model dimer system, our study has shed light on the solid-state emission properties of HTANGO. We have found that the emission maximum in the solid state is red-shifted compared to the solution phase, indicating the formation of π-stack dimers. The potential energy surfaces of these dimers reveal two distinct minima in the excited singlet (S_1) and triplet (T_1) states at angles of 10° and 60°. The energy of the T_1 state at 10° agrees well with the reported emission spectrum, highlighting the influence of crystal packing on the excited state properties.

Overall, our computational investigation provides valuable insights into the excited state properties of HTANGO, offering a deeper understanding of its potential as an ORTP dye and the influence of crystal packing on its emission characteristics.

ASSOCIATED CONTENT

Supporting Information

The Supporting Information is available free of charge at https://pubs.acs.org/doi/10.1021/acs.jctc.3c01220.

Computational details, Hamiltonian parameters, plots of the singlet and triplet potential energy surfaces, and molecular dynamics (PDF)

AUTHOR INFORMATION

Corresponding Author

Thomas J. Penfold − *Chemistry, School of Natural and Environmental Sciences, Newcastle University, Newcastle upon Tyne NE1 7RU, U.K.;* orcid.org/0000-0003-4490-5672; Email: tom.penfold@newcastle.ac.uk

Authors

Thomas Pope − *Chemistry, School of Natural and Environmental Sciences, Newcastle University, Newcastle upon Tyne NE1 7RU, U.K.;* orcid.org/0000-0001-7552-9812

Julien Eng − *Chemistry, School of Natural and Environmental Sciences, Newcastle University, Newcastle upon Tyne NE1 7RU, U.K.;* orcid.org/0000-0002-7118-7242

Andrew Monkman − *Department of Physics, Durham University, Durham DH1 3LE, U.K.;* orcid.org/0000-0002-0784-8640

Complete contact information is available at: https://pubs.acs.org/10.1021/acs.jctc.3c01220

Notes

The authors declare no competing financial interest.

ACKNOWLEDGMENTS

The authors acknowledge support from EPSRC Grants EP/V010573/1 and EP/T022442/1. This research made use of the Rocket High-Performance Computing service at Newcastle University.

REFERENCES

(1) Marian, C. M. Spin−orbit coupling and intersystem crossing in molecules. *Wiley Interdisciplinary Reviews: Computational Molecular Science* **2012**, *2*, 187−203.
(2) Marian, C. M. Understanding and controlling intersystem crossing in molecules. *Annu. Rev. Phys. Chem.* **2021**, *72*, 617−640.
(3) Lower, S.; El-Sayed, M. The triplet state and molecular electronic processes in organic molecules. *Chem. Rev.* **1966**, *66*, 199−241.
(4) Penfold, T. J.; Gindensperger, E.; Daniel, C.; Marian, C. M. Spin-vibronic mechanism for intersystem crossing. *Chem. Rev.* **2018**, *118*, 6975−7025.
(5) Sasikumar, D.; John, A. T.; Sunny, J.; Hariharan, M. Access to the triplet excited states of organic chromophores. *Chem. Soc. Rev.* **2020**, *49*, 6122−6140.
(6) Penfold, T.; Spesyvtsev, R.; Kirkby, O.; Minns, R.; Parker, D.; Fielding, H.; Worth, G. Quantum dynamics study of the competing ultrafast intersystem crossing and internal conversion in the "channel 3" region of benzene. *J. Chem. Phys.* **2012**, *137*, 204310.
(7) Ahmed, R.; Manna, A. K. Origins of Molecular-Twist-Triggered Intersystem Crossing in Functional Perylenediimides: Singlet−Triplet Gap versus Spin−Orbit Coupling. *J. Phys. Chem. A* **2022**, *126*, 6594−6603.
(8) Eng, J.; Penfold, T. J. Understanding and designing thermally activated delayed fluorescence emitters: beyond the energy gap approximation. *Chem. Rec.* **2020**, *20*, 831−856.
(9) Kenry; Chen, C.; Liu, B. Enhancing the performance of pure organic room-temperature phosphorescent luminophores. *Nat. Commun.* **2019**, *10*, 2111.
(10) Wu, Z.; Nitsch, J.; Marder, T. B. Persistent room-temperature phosphorescence from purely organic molecules and multi-component systems. *Advanced Optical Materials* **2021**, *9*, 2100411.
(11) Chen, C.; Chi, Z.; Chong, K. C.; Batsanov, A. S.; Yang, Z.; Mao, Z.; Yang, Z.; Liu, B. Carbazole isomers induce ultralong organic phosphorescence. *Nature materials* **2021**, *20*, 175−180.
(12) Zhao, J.; Chen, K.; Hou, Y.; Che, Y.; Liu, L.; Jia, D. Recent progress in heavy atom-free organic compounds showing unexpected intersystem crossing (ISC) ability. *Organic & biomolecular chemistry* **2018**, *16*, 3692−3701.
(13) Huang, T.; Jiang, W.; Duan, L. Recent progress in solution processable TADF materials for organic light-emitting diodes. *Journal of Materials Chemistry C* **2018**, *6*, 5577−5596.
(14) Bryden, M. A.; Zysman-Colman, E. Organic thermally activated delayed fluorescence (TADF) compounds used in photocatalysis. *Chem. Soc. Rev.* **2021**, *50*, 7587−7680.
(15) Eng, J.; Penfold, T. J. Open questions on the photophysics of thermally activated delayed fluorescence. *Communications Chemistry* **2021**, *4*, 91.
(16) Majumdar, P.; Nomula, R.; Zhao, J. Activatable triplet photosensitizers: magic bullets for targeted photodynamic therapy. *Journal of Materials Chemistry C* **2014**, *2*, 5982−5997.
(17) Yang, Y.; Guo, Q.; Chen, H.; Zhou, Z.; Guo, Z.; Shen, Z. Thienopyrrole-expanded BODIPY as a potential NIR photosensitizer for photodynamic therapy. *Chem. Commun.* **2013**, *49*, 3940−3942.
(18) Strieth-Kalthoff, F.; Glorius, F. Triplet energy transfer photocatalysis: unlocking the next level. *Chem.* **2020**, *6*, 1888−1903.
(19) Huang, L.; Cui, X.; Therrien, B.; Zhao, J. Energy-funneling-based broadband visible-light-absorbing bodipy−C60 triads and tetrads as dual functional heavy-atom-free organic triplet photosensitizers for photocatalytic organic reactions. *Chemistry−A. European Journal* **2013**, *19*, 17472−17482.
(20) Zhao, J.; Wu, W.; Sun, J.; Guo, S. Triplet photosensitizers: from molecular design to applications. *Chem. Soc. Rev.* **2013**, *42*, 5323−5351.
(21) Erbas-Cakmak, S.; Kolemen, S.; Sedgwick, A. C.; Gunnlaugsson, T.; James, T. D.; Yoon, J.; Akkaya, E. U. Molecular logic gates: the past, present and future. *Chem. Soc. Rev.* **2018**, *47*, 2228−2248.
(22) Zhao, W.; He, Z.; Tang, B. Z. Room-temperature phosphorescence from organic aggregates. *Nature Reviews Materials* **2020**, *5*, 869−885.
(23) Yang, J.; Zhen, X.; Wang, B.; Gao, X.; Ren, Z.; Wang, J.; Xie, Y.; Li, J.; Peng, Q.; Pu, K.; et al. The influence of the molecular packing on the room temperature phosphorescence of purely organic luminogens. *Nat. Commun.* **2018**, *9*, 840.
(24) Wang, Y.; Yang, J.; Tian, Y.; Fang, M.; Liao, Q.; Wang, L.; Hu, W.; Tang, B. Z.; Li, Z. Persistent organic room temperature phosphorescence: what is the role of molecular dimers? *Chemical Science* **2020**, *11*, 833−838.
(25) Zhao, W.; He, Z.; Lam, J. W.; Peng, Q.; Ma, H.; Shuai, Z.; Bai, G.; Hao, J.; Tang, B. Z. Rational molecular design for achieving persistent and efficient pure organic room-temperature phosphorescence. *Chem.* **2016**, *1*, 592−602.
(26) Turro, N. J. *Modern molecular photochemistry*; University Science Books: 1991.
(27) Minns, R.; Parker, D.; Penfold, T.; Worth, G.; Fielding, H. Competing ultrafast intersystem crossing and internal conversion in the "channel 3" region of benzene. *Phys. Chem. Chem. Phys.* **2010**, *12*, 15607−15615.
(28) McGlynn, S.; Azumi, T.; Kasha, M. External Heavy-Atom Spin—Orbital coupling effect. V. absorption studies of triplet states. *J. Chem. Phys.* **1964**, *40*, 507−515.
(29) Shao, W.; Jiang, H.; Ansari, R.; Zimmerman, P. M.; Kim, J. Heavy atom oriented orbital angular momentum manipulation in metal-free organic phosphors. *Chemical Science* **2022**, *13*, 789−797.
(30) Jankowiak, R.; Bässler, H. Deformation-induced increase of spin—orbit coupling in the benzophenone molecule. *Chemical physics letters* **1984**, *108*, 209−213.
(31) Beljonne, D.; Shuai, Z.; Pourtois, G.; Bredas, J. Spin- orbit coupling and intersystem crossing in conjugated polymers: a configuration interaction description. *J. Phys. Chem. A* **2001**, *105*, 3899−3907.
(32) Zheng, S.; Zhu, T.; Wang, Y.; Yang, T.; Yuan, W. Z. Accessing tunable afterglows from highly twisted nonaromatic organic AIEgens via effective through-space conjugation. *Angew. Chem., Int. Ed.* **2020**, *59*, 10018−10022.
(33) Baronas, P.; Komskis, R.; Tankeleviciute, E.; Adomėnas, P.; Adomėnienė, O.; Juršėnas, S. Helical molecular orbitals to induce spin−orbit coupling in oligoyne-bridged bifluorenes. *J. Phys. Chem. Lett.* **2021**, *12*, 6827−6833.
(34) Lyskov, I.; Marian, C. M. Climbing up the ladder: Intermediate triplet states promote the reverse intersystem crossing in the efficient TADF emitter ACRSA. *J. Phys. Chem. C* **2017**, *121*, 21145−21153.
(35) Dos Santos, P. L.; Ward, J. S.; Congrave, D. G.; Batsanov, A. S.; Eng, J.; Stacey, J. E.; Penfold, T. J.; Monkman, A. P.; Bryce, M. R. Triazatruxene: A Rigid Central Donor Unit for a D−A3 Thermally Activated Delayed Fluorescence Material Exhibiting Sub-Microsecond Reverse Intersystem Crossing and Unity Quantum Yield via Multiple Singlet−Triplet State Pairs. *Advanced Science* **2018**, *5*, 1700989.
(36) Eng, J.; Hagon, J.; Penfold, T. J. D−A 3 TADF emitters: the role of the density of states for achieving faster triplet harvesting rates. *Journal of Materials Chemistry C* **2019**, *7*, 12942−12952.
(37) Zhang, W.; Alonso-Mori, R.; Bergmann, U.; Bressler, C.; Chollet, M.; Galler, A.; Gawelda, W.; Hadt, R. G.; Hartsock, R. W.; Kroll, T.; et al. Tracking excited-state charge and spin dynamics in iron coordination complexes. *Nature* **2014**, *509*, 345−348.
(38) Atkins, A. J.; González, L. Trajectory surface-hopping dynamics including intersystem crossing in [Ru (bpy) 3] 2+. *J. Phys. Chem. Lett.* **2017**, *8*, 3840−3845.
(39) El-Sayed, M. Spin—orbit coupling and the radiationless processes in nitrogen heterocyclics. *J. Chem. Phys.* **1963**, *38*, 2834−2838.
(40) Penfold, T.; Worth, G. The effect of molecular distortions on spin−orbit coupling in simple hydrocarbons. *Chem. Phys.* **2010**, *375*, 58−66.

https://doi.org/10.1021/acs.jctc.3c01220
J. Chem. Theory Comput. 2024, 20, 1337−1346

(41) Hamzehpoor, E.; Perepichka, D. F. Crystal engineering of room temperature phosphorescence in organic solids. *Angew. Chem.* **2020**, *132*, 10063−10067.
(42) Ohmori, N.; Suzuki, T.; Ito, M. Why does intersystem crossing occur in isolated molecules of benzaldehyde, acetophenone, and benzophenone? *J. Phys. Chem.* **1988**, *92*, 1086−1093.
(43) Aloïse, S.; Ruckebusch, C.; Blanchet, L.; Réhault, J.; Buntinx, G.; Huvenne, J.-P. The benzophenone S1 (n, π^*)→ T1 (n, π^*) states intersystem crossing reinvestigated by ultrafast absorption spectroscopy and multivariate curve resolution. *J. Phys. Chem. A* **2008**, *112*, 224−231.
(44) Metz, S.; Marian, C. M. Modulation of Intersystem Crossing by Chemical Composition and Solvent Effects: Benzophenone, Anthrone and Fluorenone. *ChemPhotoChem.* **2022**, *6*, No. e202200098.
(45) Marazzi, M.; Mai, S.; Roca-Sanjuán, D.; Delcey, M. G.; Lindh, R.; González, L.; Monari, A. Benzophenone ultrafast triplet population: revisiting the kinetic model by surface-hopping dynamics. *J. Phys. Chem. Lett.* **2016**, *7*, 622−626.
(46) Venkatraman, R. K.; Kayal, S.; Barak, A.; Orr-Ewing, A. J.; Umapathy, S. Intermolecular hydrogen bonding controlled intersystem crossing rates of benzophenone. *J. Phys. Chem. Lett.* **2018**, *9*, 1642−1648.
(47) Yuan, W. Z.; Shen, X. Y.; Zhao, H.; Lam, J. W.; Tang, L.; Lu, P.; Wang, C.; Liu, Y.; Wang, Z.; Zheng, Q. Crystallization-induced phosphorescence of pure organic luminogens at room temperature. *J. Phys. Chem. C* **2010**, *114*, 6090−6099.
(48) Favero, L.; Granucci, G.; Persico, M. Surface hopping investigation of benzophenone excited state dynamics. *Phys. Chem. Chem. Phys.* **2016**, *18*, 10499−10506.
(49) Karak, P.; Chakrabarti, S. The influence of spin−orbit coupling, Duschinsky rotation and displacement vector on the rate of intersystem crossing of benzophenone and its fused analog fluorenone: a time dependent correlation function based approach. *Phys. Chem. Chem. Phys.* **2020**, *22*, 24399−24409.
(50) Hellwinkel, D.; Melan, M. Heteropolycyclen vom Triangulen-Typ, I. 8.12-Dihydro-4H-benzo [1.9] chinolizino [3.4. 5.6. 7-defg] acridin-trion-(4.8. 12) und 5.9-Dihydro-chino [3.2. 1-de] acridin-dion-(5.9). *Chem. Ber.* **1971**, *104*, 1001−1016.
(51) Field, J. E.; Venkataraman, D. Heterotriangulenes Structure and Properties. *Chemistry of materials* **2002**, *14*, 962−964.
(52) Yu, Y.-J.; Liu, F.-M.; Meng, X.-Y.; Ding, L.-Y.; Liao, L.-S.; Jiang, Z.-Q. Carbonyl-Containing Thermally Activated Delayed Fluorescence Emitters for Narrow-Band Electroluminescence. *Chemistry A European Journal* **2023**, *29*, No. e202202628.
(53) Zou, S.-N.; Peng, C.-C.; Yang, S.-Y.; Qu, Y.-K.; Yu, Y.-J.; Chen, X.; Jiang, Z.-Q.; Liao, L.-S. Fully Bridged Triphenylamine Derivatives as Color-Tunable Thermally Activated Delayed Fluorescence Emitters. *Org. Lett.* **2021**, *23*, 958−962.
(54) Neese, F. The ORCA program system. *Wiley Interdisciplinary Reviews: Computational Molecular Science* **2012**, *2*, 73−78.
(55) Neese, F. Software update: the ORCA program system, version 4.0. *Wiley Interdisciplinary Reviews: Computational Molecular Science* **2018**, *8*, No. e1327.
(56) Neese, F.; Wennmohs, F.; Becker, U.; Riplinger, C. The ORCA quantum chemistry program package. *J. Chem. Phys.* **2020**, *152*, 224108.
(57) Hellweg, A.; Hättig, C.; Höfener, S.; Klopper, W. Optimized accurate auxiliary basis sets for RI-MP2 and RI-CC2 calculations for the atoms Rb to Rn. *Theor. Chem. Acc.* **2007**, *117*, 587−597.
(58) Weigend, F. Accurate Coulomb-fitting basis sets for H to Rn. *Physical chemistry chemical physics* **2006**, *8*, 1057−1065.
(59) Tomasi, J.; Mennucci, B.; Cammi, R. Quantum mechanical continuum solvation models. *Chem. Rev.* **2005**, *105*, 2999−3094.
(60) Perdew, J. P.; Burke, K.; Ernzerhof, M. Generalized gradient approximation made simple. *Physical review letters* **1996**, *77*, 3865.
(61) Adamo, C.; Barone, V. Toward reliable density functional methods without adjustable parameters: The PBE0 model. *J. Chem. Phys.* **1999**, *110*, 6158−6170.
(62) Grimme, S. Semiempirical GGA-type density functional constructed with a long-range dispersion correction. *Journal of computational chemistry* **2006**, *27*, 1787−1799.
(63) Grimme, S.; Ehrlich, S.; Goerigk, L. Effect of the damping function in dispersion corrected density functional theory. *Journal of computational chemistry* **2011**, *32*, 1456−1465.
(64) Hirata, S.; Head-Gordon, M. Time-dependent density functional theory within the Tamm−Dancoff approximation. *Chem. Phys. Lett.* **1999**, *314*, 291−299.
(65) Cederbaum, L.; Köppel, H.; Domcke, W. Multimode vibronic coupling effects in molecules. *Int. J. Quantum Chem.* **1981**, *20*, 251−267.
(66) Köppel, H.; Domcke, W.; Cederbaum, L. S. *Conical intersections: electronic structure, dynamics and spectroscopy*; World Scientific: 2004; pp 323−367.
(67) Raab, A.; Worth, G. A.; Meyer, H.-D.; Cederbaum, L. Molecular dynamics of pyrazine after excitation to the S 2 electronic state using a realistic 24-mode model Hamiltonian. *J. Chem. Phys.* **1999**, *110*, 936−946.
(68) Köppel, H.; Cederbaum, L.; Domcke, W. Interplay of Jahn−Teller and pseudo-Jahn−Teller vibronic dynamics in the benzene cation. *J. Chem. Phys.* **1988**, *89*, 2023−2040.
(69) Mahapatra, S.; Worth, G. A.; Meyer, H.-D.; Cederbaum, L.; Köppel, H. The A2E/B2B2 photoelectron bands of allene beyond the linear coupling scheme: An ab initio dynamical study including all fifteen vibrational modes. *J. Phys. Chem. A* **2001**, *105*, 5567−5576.
(70) Worth, G. A.; Welch, G.; Paterson, M. J. Wavepacket dynamics study of cr (co) 5 after formation by photodissociation: relaxation through an ($e \otimes a$) $\otimes$ *e*Jahn−Teller conical intersection. *Mol. Phys.* **2006**, *104*, 1095−1105.
(71) Plasser, F.; Gómez, S.; Menger, M. F.; Mai, S.; González, L. Highly efficient surface hopping dynamics using a linear vibronic coupling model. *Phys. Chem. Chem. Phys.* **2019**, *21*, 57−69.
(72) Eng, J.; Thompson, S.; Goodwin, H.; Credgington, D.; Penfold, T. J. Competition between the heavy atom effect and vibronic coupling in donor−bridge−acceptor organometallics. *Phys. Chem. Chem. Phys.* **2020**, *22*, 4659−4667.
(73) Pápai, M.; Penfold, T. J.; Møller, K. B. Effect of tert-butyl functionalization on the photoexcited decay of a Fe (II)-N-heterocyclic carbene complex. *J. Phys. Chem. C* **2016**, *120*, 17234−17241.
(74) Zobel, J. P.; Heindl, M.; Plasser, F.; Mai, S.; González, L. Surface hopping dynamics on vibronic coupling models. *Accounts of chemical research* **2021**, *54*, 3760−3771.
(75) Zobel, J. P.; Bokareva, O. S.; Zimmer, P.; Wölper, C.; Bauer, M.; González, L. Intersystem crossing and triplet dynamics in an iron (II) N-heterocyclic carbene photosensitizer. *Inorganic chemistry* **2020**, *59*, 14666−14678.
(76) de Souza, B.; Farias, G.; Neese, F.; Izsak, R. Predicting phosphorescence rates of light organic molecules using time-dependent density functional theory and the path integral approach to dynamics. *J. Chem. Theory Comput.* **2019**, *15*, 1896−1904.
(77) Penfold, T. J.; Eng, J. Mind the GAP: quantifying the breakdown of the linear vibronic coupling Hamiltonian. *Phys. Chem. Chem. Phys.* **2023**, *25*, 7195−7204.
(78) Worth, G. Quantics: A general purpose package for Quantum molecular dynamics simulations. *Comput. Phys. Commun.* **2020**, *248*, 107040.
(79) Beck, M. H.; Jäckle, A.; Worth, G. A.; Meyer, H.-D. The multiconfiguration time-dependent Hartree (MCTDH) method: a highly efficient algorithm for propagating wavepackets. *Physics reports* **2000**, *324*, 1−105.
(80) Meyer, H.-D.; Manthe, U.; Cederbaum, L. S. The multi-configurational time-dependent Hartree approach. *Chem. Phys. Lett.* **1990**, *165*, 73−78.
(81) Ahmad, S. A.; Eng, J.; Penfold, T. J. Rapid predictions of the colour purity of luminescent organic molecules. *Journal of Materials Chemistry C* **2022**, *10*, 4785−4794.

https://doi.org/10.1021/acs.jctc.3c01220
J. Chem. Theory Comput. 2024, 20, 1337−1346

(82) Ma, S.; Du, S.; Pan, G.; Dai, S.; Xu, B.; Tian, W. Organic molecular aggregates: From aggregation structure to emission property. *Aggregate* **2021**, *2*, No. e96.
(83) Capano, G.; Chergui, M.; Rothlisberger, U.; Tavernelli, I.; Penfold, T. J. A quantum dynamics study of the ultrafast relaxation in a prototypical Cu (I)−phenanthroline. *J. Phys. Chem. A* **2014**, *118*, 9861−9869.

https://doi.org/10.1021/acs.jctc.3c01220
J. Chem. Theory Comput. 2024, 20, 1337−1346